



## Biomechanics of single cortical neurons

Kristin B. Bernick<sup>a</sup>, Thibault P. Prevost<sup>b</sup>, Subra Suresh<sup>a,b</sup>, Simona Socrate<sup>c,\*</sup>

<sup>a</sup> Department of Biological Engineering, Massachusetts Institute of Technology, 77 Massachusetts Avenue, Cambridge, MA 02139-4307, USA

<sup>b</sup> Department of Materials Science and Engineering, Massachusetts Institute of Technology, 77 Massachusetts Avenue, Cambridge, MA 02139-4307, USA

<sup>c</sup> Division of Health Sciences and Technology, Massachusetts Institute of Technology, 77 Massachusetts Avenue, Cambridge, MA 02139-4307, USA

### ARTICLE INFO

#### Article history:

Received 15 July 2010

Received in revised form 8 October 2010

Accepted 19 October 2010

Available online 3 December 2010

#### Keywords:

Atomic force microscopy

Neuron

Cell mechanics

Constitutive modeling

Finite elements

### ABSTRACT

This study presents experimental results and computational analysis of the large strain dynamic behavior of single neurons in vitro with the objective of formulating a novel quantitative framework for the biomechanics of cortical neurons. Relying on the atomic force microscopy (AFM) technique, novel testing protocols are developed to enable the characterization of neural soma deformability over a range of indentation rates spanning three orders of magnitude, 10, 1, and 0.1  $\mu\text{m s}^{-1}$ . Modified spherical AFM probes were utilized to compress the cell bodies of neonatal rat cortical neurons in load, unload, reload and relaxation conditions. The cell response showed marked hysteretic features, strong non-linearities, and substantial time/rate dependencies. The rheological data were complemented with geometrical measurements of cell body morphology, i.e. cross-diameter and height estimates. A constitutive model, validated by the present experiments, is proposed to quantify the mechanical behavior of cortical neurons. The model aimed to correlate empirical findings with measurable degrees of (hyper)elastic resilience and viscosity at the cell level. The proposed formulation, predicated upon previous constitutive model developments undertaken at the cortical tissue level, was implemented in a three-dimensional finite element framework. The simulated cell response was calibrated to the experimental measurements under the selected test conditions, providing a novel single cell model that could form the basis for further refinements.

© 2010 Acta Materialia Inc. Published by Elsevier Ltd. All rights reserved.

## 1. Introduction

Traumatic brain injury (TBI) is a major cause of death and morbidity in the USA, affecting some 2 million civilians each year [1] and an estimated 20% of the 1.6 million veteran population returning from Iraq and Afghanistan [2,3]. While the most common damage occurrences leading to mild or moderate forms of TBI (e.g. motor vehicle accidents or falls [4–6], sports concussions [7–9], and blast exposures [6,10–12]) have been widely acknowledged and thoroughly reviewed, the etiology of the ensuing cognitive, behavioral or neuropsychological disorders/impairments (e.g. memory loss, language difficulties, concentration deficiencies, behavioral abnormalities and/or depression) remains poorly understood. In particular, little is known about the multiple damage mechanisms suspected to unfold at the neural cell level in the seconds to hours (and probably days) following initial mechanical insult(s) to the brain, and likely to result in cell/tissue alteration. One line of approach towards elucidating some of the key damage mechanisms involved in TBI relies on addressing two distinct, yet interrelated, questions: (1) how mechanical transients

applied to the organ boundary (head) translate into local stress–strain (force–displacement) distribution maps at the mesoscopic tissue level and microscopic cell level; (2) how the cell machinery responds to these mechanical stimuli. An improved quantitative knowledge of material properties at the individual central nervous system (CNS) cell level is necessary to understand the former on a quantitative basis and to better characterize the latter in a controlled environment. Such characterization inevitably calls for measurable external mechanical inputs (e.g. pressure waves, imposed deformation profiles) to be applied to the boundary of in vitro cell systems (e.g. two-dimensional (2D)/three-dimensional (3D) cell culture constructs, organotypic tissue slices) in a reproducible manner so that the latter inputs may systematically be associated with reliable estimates of force and deformation magnitudes at the single cell level.

Probing the mechanical properties of individual cells has been made possible in recent years through the advent of novel testing techniques (for a review see, for example, Bao and Suresh [13], Van Vliet et al. [14], and Suresh [15]), including magnetic twisting cytometry [16–19], atomic force microscopy (AFM) [20–25], micropipette aspiration [26–31], optical tweezing and stretching [32–35], and microplate rheometry [36–38]. The last three techniques, which have been successfully employed to characterize the deformability of certain cell types in suspension (e.g. red blood

\* Corresponding author. Tel.: +1 617 452 2689; fax: +1 617 258 8742.

E-mail address: [ssocrate@mit.edu](mailto:ssocrate@mit.edu) (S. Socrate).

cells [28,34], white blood cells [26,29], Müller glial cells [35], chondrocytes [31], myofibroblasts [27], and pancreatic cancer cells [38]), may not be easily applied to CNS neuronal cultures because neurons in vitro form intricate networks of adherent cells interconnected via multiple processes whose continuous growth and viable maintenance require the support of a substrate. Magnetic twisting cytometry is a powerful measurement technique providing local material properties at the membrane level but is not suited to examine global properties at the cell body level. AFM, originally developed to image surfaces of inorganic materials at atomic resolution [39], has proven to be a highly versatile testing tool in mechanobiology, enabling the measurement of material properties at the cell/subcell level over a large range of forces (from pico- to nanonewton levels), speeds (from quasistatic to dynamic load levels), and length scales (from nano- to micrometers) via a variety of tip geometries [40]. The diversity in available AFM tip geometries allows a range of experiments to be performed under various loading conditions: sharp tips may probe local properties at the cytoskeletal level while large spheres may provide global “homogenized” properties at the whole cell level. Although widely used to characterize the mechanical response of numerous cell types, including fibroblasts [20], leukocytes [24], cardiac myocytes [23], and blood cells [22,25], AFM has been infrequently utilized to examine the response of neural cells. To our knowledge, only Lu et al. [35] have reported dynamic mechanical measurements on single CNS neurons, with measurements conducted in the linear infinitesimal strain regime only. Elastic storage and viscous loss moduli were extracted from the force–displacement output of oscillating 3  $\mu\text{m}$  spherical AFM probes actuated to small indentation depths at the cell surface. These measurements, aimed at characterizing some of the local viscoelastic properties of neural cells, could not provide significant insights into the global mechanical response of single neural cell bodies, nor were they directed at investigating the mechanical non-linearities observed at finite deformation typical of the anticipated cell response in TBI cases, for which strains larger than 15–20% may be expected [41–44].

AFM mechanical measurements conducted at the (whole) cell level on other cell types have been interpreted quantitatively with the aid of various continuum models. The modeling approaches most commonly used borrow their formulation from the contact theory developed by Hertz for linear elastic materials [20,35,45–47], many of which typically incorporate time dependencies inherent in the cell response [20,35]. The Hertz contact theory, however, relies on highly reductive assumptions, including linearity, homogeneity, infinitesimal deformation, and infinite substrate dimensions, all of which are unlikely to hold for biological cell systems submitted to mechanical transients. In order to address some of these limitations, investigators have proposed alternative continuum approaches integrating part of the complexities observed in the mechanical response of biological cells. These approaches include piecewise linear elastic variations [48], linear hyperelastic/viscoelastic composite material formulations [25,49,50], and bi-phasic linear elastic constitutive relations [51,52]. More complex variations borrow elements from continuum and piecewise continuum models [53]. While successful at capturing specific quantitative features of the cell response under selected test conditions, these formulations do not account for the combined strain and strain–rate nonlinear dependencies inherent in the cell behavior, as substantiated by a growing body of experimental observations [23,37,54].

The study described here provides, to our knowledge, the first reported set of experimental measurements characterizing the large strain, nonlinear dynamic response of single cortical neurons at the soma level. The AFM “compression” tests performed on individual cell bodies via microsphere-modified cantilevers consisted of load–unload cyclic sequences over three orders of displacement

rate magnitude. The mechanical data collected were further analyzed with the support of a continuum model allowing for large strain kinematics simulations of the cell behavior. The proposed model lays the foundation for further developments and refinements as more experimental results become available on a variety of related cell types and under different in vitro testing conditions.

## 2. Materials and methods

### 2.1. Cell culture

Primary neuronal cultures were prepared from cerebral cortices of postnatal day 1 Sprague–Dawley rats (Charles River Laboratories, Wilmington, MA). Tissue was provided by the laboratory of Professor Sebastian Seung, following a protocol approved by the Committee on Animal Care at the Massachusetts Institute of Technology. The dissociation procedure was adapted from a protocol detailed elsewhere [55]. Briefly, isolated cortices were minced, rinsed three times in modified Hank’s buffered salt solution (HBSS) containing 25 mM HEPES, and digested for 12 min at 37 °C with an enzyme solution containing 1 mM L-cysteine, 0.5 mM EDTA, 1.5 mM  $\text{CaCl}_2$ , 200 U papain (Sigma P3125), and 1  $\mu\text{g ml}^{-1}$  DNase (Sigma) in modified HBSS. Tissue pieces were rinsed twice in culture medium (neurobasal medium supplemented with B27 and Glutamax (Invitrogen, 21103049, 17504044, 35050061)) and gently triturated in 1 mL ice-cold culture medium through 1 mL pipette tips. The resulting suspension was passed through a 70  $\mu\text{m}$  cell strainer (BD Falcon 352350) and subsequently centrifuged at 20g for 7 min. The cell pellet was resuspended in culture medium prior to plating at  $\sim 10^4$  cells  $\text{ml}^{-1}$  density on 35 mm poly-D-lysine (Sigma P7886) coated coverslips (Carolina Biological Supply, Burlington, NC). Cultures were maintained at 37 °C in a 5%  $\text{CO}_2$  humidified atmosphere. About 1 h after plating cultures were rinsed to remove debris and non-adherent cells. About 3 days after plating half of the medium was replaced. AFM measurements were initiated after 5 days in culture, i.e. when plated neurons had reached maturation with well-extended processes.

Neural cell viability was assessed on representative samples via a standard Live/Dead cytotoxicity assay (Invitrogen L-3224) to ensure that the cells in culture were healthy at the time of testing. The cytoplasm of live cells and the nucleus of dead cells were stained with 2  $\mu\text{M}$  calcein AM and 2  $\mu\text{M}$  ethidium homodimer-1, respectively. Cell cultures were found to be viable after 5 days incubation (Fig. 1A).

Immunocytochemistry assays were also performed to ascertain neural cell types. Anti- $\beta$ -III tubulin (Abcam ab24629) and anti-glial fibrillary acidic protein (GFAP) (Abcam ab4648) were used to identify neurons and astrocytes, respectively. The cultures obtained for this study were confirmed to be predominantly composed of neurons, showing staining for  $\beta$ -III tubulin (Fig. 1C) and not GFAP (Fig. 1D). During AFM experiments neurons were identified by their characteristic morphology using a light microscope.

### 2.2. Atomic force microscopy

#### 2.2.1. Dynamic load–unload tests

Somata of single neurons were indented via an atomic force microscope (MFP 3D, Asylum Research, Santa Barbara, CA) mounted on an inverted optical microscope (Axio Observer D1, Carl Zeiss MicroImaging, Thornwood, NY). The mechanical probes selected for the tests were polystyrene spheres (45  $\mu\text{m}$  diameter Polybead® Microspheres, Polysciences Inc., Warrington, PA) mounted on tipless, triangular shaped silicon nitride cantilevers (Veeco Probes NP-OW, 0.06  $\text{N m}^{-1}$ , Nanoworld PNP-TR-TL, 0.08  $\text{N m}^{-1}$ ). The microspheres were deliberately chosen larger

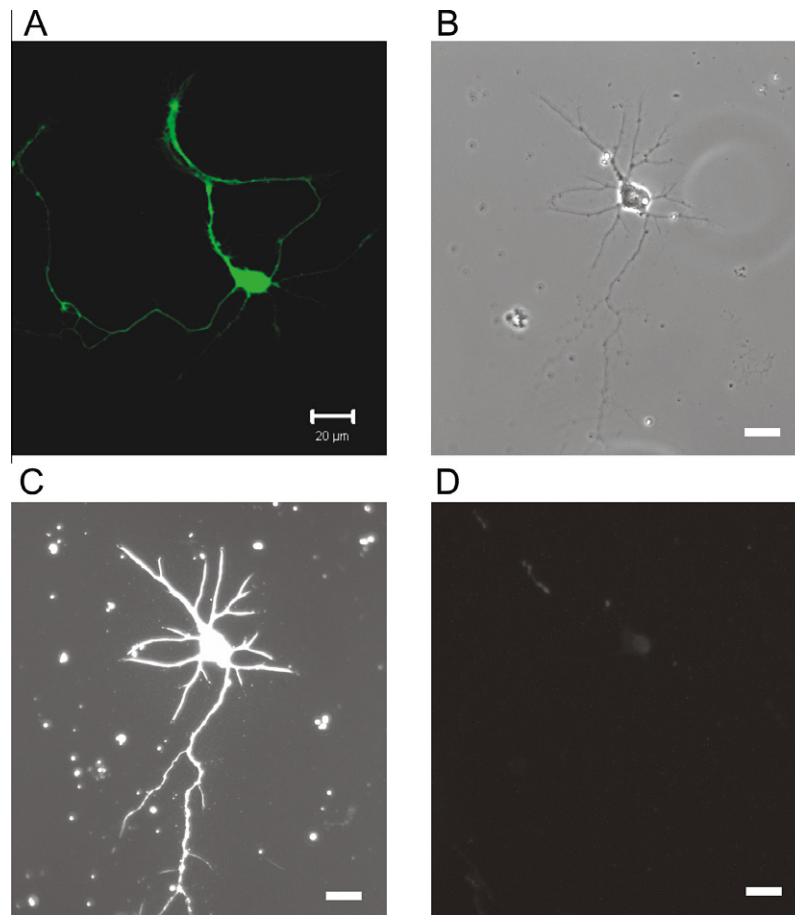


**Fig. 1.** (A) Viability assay: neuron stained with calcein-AM to verify cell viability after 5 days culture (time of a typical AFM experiment). (B–D) Immunostaining verifying cell type: (B) bright field image of neuron; (C)  $\beta$ -III tubulin staining indicating mature neuron; (D) GFAP staining showing glial marker not present in culture. Scale bars 20  $\mu$ m.

than the cell soma in order to approximate loading conditions close to those prevailing in “uniaxial compression” experiments. The microspheres were attached to the end of the silicon nitride probes using UV curable Loctite 3211 glue and allowed to cure for 1 h under UV light. The size and positioning of the bead were verified for one representative sample via scanning electron microscopy (Fig. 2A). All tests, which lasted less than 2 h, were conducted in culture medium at 37 °C in a fluid cell chamber (BioHeater™, Asylum Research, Santa Barbara, CA). Prior to testing, the spherical probe sitting above the sample was lowered into the medium and allowed to reach thermal equilibrium for about 30 min. Calibration of the spring constant was achieved for each probe using the thermal method [56]. Cell viability was checked by visual inspection through a bright field optical microscope during testing. Neurons were found to have adhered well and were visually healthy throughout the test procedure. No fluorescence staining of the cells to be indented was performed as the addition of chemical dyes could have induced material property changes.

All tests were conducted under bright field optical microscopy (Fig. 2B). The cantilever tip was positioned on top of the cell body via manual actuation of the micrometric screws controlling the horizontal x–y positioning of the AFM optical stage. The center of the cell body was aligned with the vertical z-axis of the indenting probe through the 20 $\times$  magnification objective of the microscope (Fig. 2C). The indentation test sequence, implemented as a custom routine in Igor Pro software (WaveMetrics, Portland, OR), consisted of an approach phase at 0.3  $\mu$ m s<sup>−1</sup> to a 0.3 nN contact force target (corresponding to an indentation depth of roughly 50–200 nm) followed by a 15 s dwell phase in contact with the cell

body, and a subsequent series of load–unload segments at 10, 1, and 0.1  $\mu$ m s<sup>−1</sup> to 2  $\mu$ m depth followed by a 120 s relaxation segment (Fig. 2D). The relaxation segment consisted of a 10  $\mu$ m s<sup>−1</sup> loading ramp to a target indentation depth of 2  $\mu$ m held for 120 s. Note that at 2  $\mu$ m indentation depth the influence of the nucleus on the measured cell response can no longer be neglected. The properties collected should therefore be viewed as global, “homogenized” properties of the whole cell body. As cells may migrate, reorganize their cytoskeleton, and respond actively to external forces on timescales of seconds, a small population of neurons ( $n = 10$ ) was tested in the reverse order of deformation rate, i.e. 0.1, 1 and 10  $\mu$ m s<sup>−1</sup>, to assess whether such cell activation processes could contribute significantly to the strain rate effects measured. The loading rates were selected to span the broadest range of deformation speeds compatible with the MFP 3D capabilities and the physical limitations pertaining to the test configuration (e.g. inertial effects, hydrodynamic perturbations).

#### 2.2.2. Contact point and cell size estimate

To account for some variations in the neural cell body size observed within and across cultures, height and “cross-diameter” estimates were collected for each cell body indented and subsequently incorporated in the 3D finite element simulations. The characteristic cross-sectional diameter, derived from the optical microscope photographs taken at the time of indentation (see, for example, Fig. 2B), was computed as the geometric mean between the largest and smallest edge to edge measured distances:  $\sqrt{d_{\max} \cdot d_{\min}}$ . Height estimates were obtained after completion of the indentation test, following a procedure adapted from previous

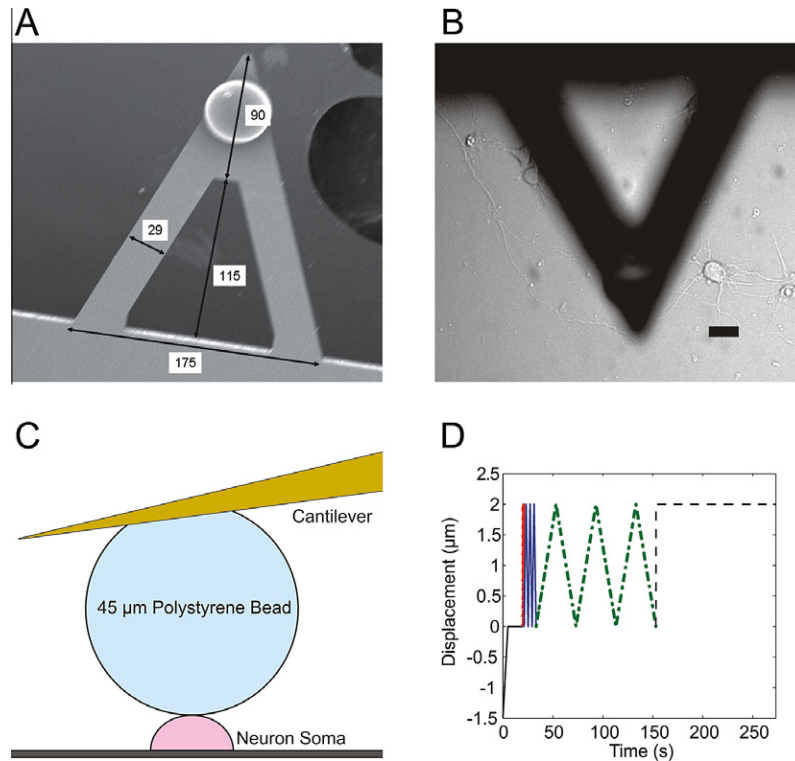


**Fig. 2.** (A) SEM image of the tipless cantilever with attached 45  $\mu\text{m}$  polystyrene sphere (dimensions in  $\mu\text{m}$ ). (B) Bright field image of the AFM tip with a bead adjacent to the neuron to be indented. Scale bar 20  $\mu\text{m}$ . (C) Schematic of the AFM experimental set-up – polystyrene bead compressing the cell body of a neuron plated on glass. (D) AFM testing procedure: sample approach, pre-load (black solid), sequences of load–unload segments at 10 (red dot), 1 (blue solid), and 0.1  $\mu\text{m s}^{-1}$  (green dash-dot), followed by stress–relaxation (black dash).

cell height determination methods [25,46]. Briefly, the cell body and two or three adjacent glass sites were successively indented at  $10 \mu\text{m s}^{-1}$  extension/retraction rate to a target force of 4.5 nN. The differences in piezo positions at contact between the cantilever and the cell body or glass substrate were retrieved from the indentation curves to derive an estimate of the cell height (Fig. 3). The glass–cantilever contact point was determined as the intersection between the pre- and post-contact linear fit to the measured force–displacement indentation responses, whereas the cell–

cantilever contact point was recovered following a hierarchical Bayesian approach detailed in Section 6.1 of Rudoy et al. [57]. Briefly, the contact point and the pre- and post-contact regression coefficients were inferred, following Gibbs sampling techniques, from statistical distributions motivated by physical arguments. The post-contact force–displacement response in the small penetration depth regime was assumed to obey a polynomial law as predicted by the Hertz model for the response of an elastic substrate to indentation by a rigid sphere (i.e.  $F \propto \delta^{3/2}$ , where  $F$  is the indenter force and  $\delta$  is the indentation depth). The height determination procedure was implemented in a MATLAB routine.

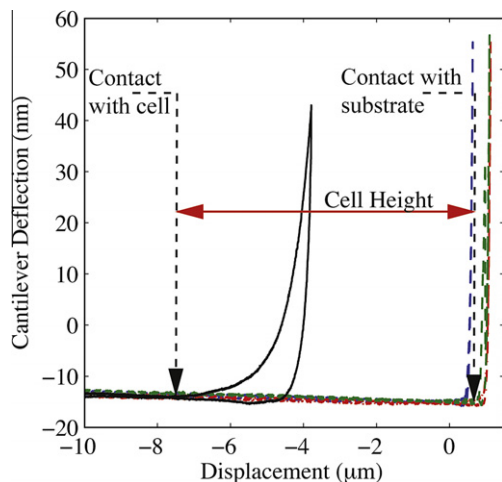


**Fig. 3.** Cell height determination procedure: the cell (black solid) and glass substrate (red, blue, green dash) indentation curves were used to retrieve relative piezo positions associated with contact events between cell/glass and cantilever, thereby providing an estimate of the cell height.

### 2.3. Modeling: finite element simulations

The mechanical data gathered on single neural somata were interpreted with the aid of a finite element framework simulating the experimental testing conditions. The continuum formulation selected for the homogenized “material properties” of the cell response is predicated upon the modeling framework developed in our recent study of the dynamic (macroscopic) behavior of porcine cortical tissue in vitro [58]. This formulation exhibits rheological features (e.g. rate effects, non-linearities, conditioning, and hysteresis) similar to those observed at the single cell level. Briefly, the selected model comprises a hyperelastic network (A) accounting for the instantaneous response of the material and a viscoelastic resistance (BCDE) encompassing the strain rate/time effects prevalent at short (B) and long (CDE) timescales. A schematic of the rheological model is provided in Fig. 4A. As the model is intended to describe the cell response to large deformations, it is cast within a large strain kinematics framework, using the concepts and standard notation of modern continuum mechanics (see, for example, Gurtin [59] or Holzapfel [60]).



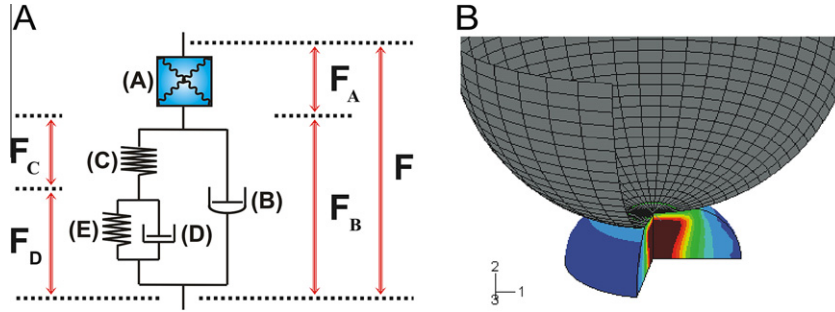


**Fig. 4.** (A) Schematic of the large strain kinematics rheological model used to capture the homogenized material response of the neuron in Abaqus. Material parameters obtained by fitting the force-indentation response to the average experimental response were found to be:  $\mu_0 = 16$  Pa,  $\lambda_L = 1.05$ ,  $G_0 = 75$  Pa,  $G_\infty = 40$  Pa,  $\eta = 3000$  Pa s,  $\sigma_0 = 0.005$  Pa, and  $n = 1$ .  $K$  was held constant at 10,000 Pa. (B) Contour plot of von Mises stress levels in a representative finite element simulation of cell response to AFM compression.

Following Lee's decomposition [61], the total deformation gradient is expressed as:

$$\mathbf{F} = \mathbf{F}_A \cdot \mathbf{F}_B, \quad (1)$$

where  $\mathbf{F}_A$  and  $\mathbf{F}_B$  represent, respectively, the elastic (instantaneous) and viscoelastic (isochoric) components of cell deformation. The viscoelastic response of the cell is captured by the combination of a nonlinear short-term viscous element (B) and a linear viscoelastic backstress network (CDE). With regard to the backstress network, the viscoelastic deformation gradient  $\mathbf{F}_B$  is further decomposed as:

$$\mathbf{F}_B = \mathbf{F}_C \cdot \mathbf{F}_D, \quad (2)$$

where the linear viscous element (D) models the long-term relaxation of the backstress contribution. Both  $\mathbf{F}_C$  and  $\mathbf{F}_D$  are taken to be isochoric. The correspondence between deformation gradients and idealized rheological network components is shown in Fig. 4A.

The Cauchy stress  $\mathbf{T}_A$  developed within the material is decomposed into its hydrostatic and deviatoric components:

$$\mathbf{T}_A = \mathbf{T}_h + \mathbf{T}_d, \quad (3)$$

where the hydrostatic component  $\mathbf{T}_h$  and the deviatoric component  $\mathbf{T}_d$  are physically associated with the deformation mechanisms prevailing in bulk and in shear.

The hydrostatic component  $\mathbf{T}_h$  is obtained in terms of the volumetric jacobian,  $J = \det(\mathbf{F}) = \det(\mathbf{F}_A)$ , according to the constitutive relationship:

$$\mathbf{T}_h = K \cdot \ln(J) \cdot \mathbf{1}, \quad (4)$$

where  $K$  is the small strain bulk modulus and  $\mathbf{1}$  is the second order identity tensor. The deviatoric component  $\mathbf{T}_d$  is obtained in terms of the isochoric component of the elastic left Cauchy–Green tensor,  $\bar{\mathbf{B}}_A = J^{-2/3} \cdot \mathbf{F}_A \cdot \mathbf{F}_A^T$ , following a formulation derived from the freely jointed eight chain model for macromolecular elastic networks [62]:

$$\mathbf{T}_d = \frac{\mu_0}{J} \cdot \frac{\lambda_L}{\lambda} \cdot L^{-1} \left( \frac{\lambda}{\lambda_L} \right) \cdot (\bar{\mathbf{B}}_A - \lambda^2 \mathbf{1}), \quad (5)$$

$$\lambda^2 = \frac{1}{3} \text{tr}(\bar{\mathbf{B}}_A),$$

$$\mathcal{L}(\beta) = \coth(\beta) - \frac{1}{\beta},$$

where  $\mu_0$  and  $\lambda_L$  are model parameters which scale, respectively, with the initial shear modulus and the limiting extensibility of the network.  $\mathcal{L}$  denotes the Langevin function.

The evolution of the viscoelastic component of the deformation gradient  $\mathbf{F}_B$  is constitutively prescribed through the nonlinear rep-

tation-based viscous element (B), adapted from Bergstrom and Boyce [63]. The deformation gradient time derivative  $\dot{\mathbf{F}}_B = \mathbf{F}_A^{-1} \cdot \dot{\mathbf{D}}_B \cdot \mathbf{F}$  is obtained by aligning the stretching tensor  $\dot{\mathbf{D}}_B$  with the direction of the (deviatoric) driving stress  $\mathbf{T}_B = \mathbf{T}_d - \mathbf{T}_C$ , where  $\mathbf{T}_C$  is the backstress from element (C), through the constitutive relationship:

$$\dot{\mathbf{D}}_B = \dot{\gamma}_B \cdot \tilde{\mathbf{N}}_B = \dot{\gamma}_B \cdot \frac{\mathbf{T}'_B}{\sqrt{\text{tr}(\mathbf{T}_B'^2)}} = \dot{\gamma}_0 f_R \left( \frac{\sqrt{\mathbf{T}'_B : \mathbf{T}'_B}}{\sqrt{2}\sigma_0} \right)^n \cdot \frac{\mathbf{T}'_B}{\sqrt{\text{tr}(\mathbf{T}_B'^2)}}, \quad (6)$$

$$f_R = \frac{\alpha^2}{(\alpha + \sqrt{\text{tr}(\mathbf{F}_B \mathbf{F}_B^T)/3} - 1)^2} \quad (7)$$

where  $\dot{\gamma}_0$  is a dimensional scaling constant ( $\dot{\gamma}_0 = 10^{-4} \text{ s}^{-1}$ ). The rep-  
tation factor,  $f_R$ , accounts for the increasing resistance to viscous flow observed in macromolecular networks for increasing levels of accumulated viscous deformation. The factor  $\alpha$  is a small constant introduced to eliminate the singularity at  $\mathbf{F}_B = \mathbf{1}$ , and is set to  $\alpha = 0.005$ , as in the previous tissue study [58]. The rate sensitivity exponent  $n$  and the strength parameter  $\sigma_0$  are material properties.

The (deviatoric) backstress  $\mathbf{T}_C$  is obtained from the standard linear solid network (CDE) as further detailed in [58]. Briefly, the stress in the elastic elements, (C) and (E), is taken to scale linearly with the deviator of the respective Hencky strains through shear moduli  $G_0$  and  $G_\infty$ . The stretching tensor  $\tilde{\mathbf{D}}_D = \mathbf{F}_C \cdot \mathbf{F}_D \cdot \mathbf{F}_B^{-1}$  in the viscous element (D) is taken to scale linearly with the driving stress in element (D) through a viscosity  $\eta$ . Conceptually, element (C) is associated with short-term dissipation mechanisms, while the linear element (E) captures the long-term partial relaxation of the backstress.

A mechanistic interpretation of the material parameters is detailed in Prevost et al. [58], and can be briefly summarized as follows.

- $K$  measures the small strain resistance to volumetric deformation (bulk modulus).
- $\mu_0$  and  $\lambda_L$  mediate the instantaneous (elastic) nonlinear response of the cell in shear. More specifically,  $\mu_0$  correlates with the low strain instantaneous shear response and  $\lambda_L$  correlates with a limiting stretch associated with a marked increase in resistance to deformation.
- $G_0$ ,  $G_\infty$ , and  $\eta$  address the time-dependencies unfolding on the medium and long time scales. More specifically, the ratio  $\tau_\infty = \eta/G_\infty$  scales with the characteristic long-term relaxation time, while  $G_0$  relates to the short-term “backstress” stiffness of the material, modulating the recovery of viscous deformation

at higher rates of loading. By neglecting the compliance of the nonlinear instantaneous elastic response, an equilibrium (long-term) shear modulus can be estimated as  $G_{eq} = (1/G_0 + 1/G_\infty)^{-1}$ .

- $\sigma_0$  and  $n$  address the time dependencies unfolding on short timescales. More specifically,  $\sigma_0$  relates to the resistance to viscous deformation in the nonlinear viscous element and  $n$  represents the strain rate sensitivity of the viscous resistance. For  $n \approx 1$ , and negligible accumulated viscous deformation, a single short-term characteristic time for viscous relaxation can be estimated as  $\tau_0 = (\sigma_0/G_0)(\dot{\gamma}_0^{-1})$ . For  $n \neq 1$  the nonlinear element captures the effects of superimposing stress-activated viscous mechanisms, and a single time constant cannot be meaningfully defined.

Note that the long-term dissipation mechanisms are captured mainly through a single retardation time provided by the standard linear solid element (CDE). Although sufficient to account for the essential features of the cell relaxation behavior (as measured under the selected test conditions of the present study), the current formulation may require some refinements (e.g. the introduction of additional Kelvin-type viscoelastic components) to encompass

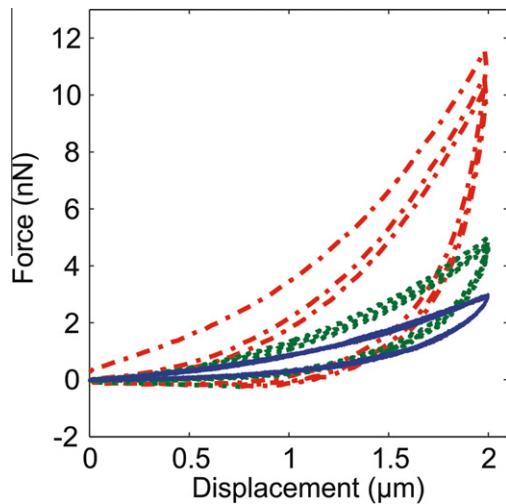


**Fig. 5.** AFM data for a representative neuron of diameter 14.2  $\mu\text{m}$  and height 7.6  $\mu\text{m}$ . Force versus displacement response at the three consecutive loading rates of 10 (red dash-dot), 1 (green dot), and 0.1  $\mu\text{m s}^{-1}$  (blue solid).

the broader spectrum of relaxation mechanisms that are likely to unfold under more complex loading conditions. Further details on the constitutive equations, and a review of the main alternative modeling approaches developed within the brain biomechanics community at the continuum tissue level, are provided in Prevost et al. [58].

The constitutive model was implemented as a user-defined material subroutine in the finite element software Abaqus (Simulia, Providence, RI). An axisymmetric representation was selected for the test configuration, as shown in Fig. 4B. The cell body was idealized as a half oblate spheroid while the indenting probe was modeled as a (rigid) sphere. Frictionless contact was enforced between the two. The underlying glass substrate was considered rigid, in slipless contact with the cell. The physical dimensions of the soma were taken to match the measured estimates, cross-diameter and height, obtained for each cell. The entire loading history (approach, dwell, dynamic load-unload, relaxation) was simulated in Abaqus and the material model parameters for each (homogenized) cell were determined by fitting the experimental responses, where the quality of the fit was estimated based on the error measure:

$$\text{Error} = \frac{\sqrt{\langle (F_{\text{simul}} - F_{\text{exp}})^2 \rangle}}{F_{\text{exp}}^{\text{max}}}$$

$F_{\text{simul}}$  and  $F_{\text{exp}}$  refer to the discrete time vectors for the simulated and measured indenter forces, respectively, and  $F_{\text{exp}}^{\text{max}}$  corresponds to the maximum reaction force as measured experimentally at the highest ( $10 \mu\text{m s}^{-1}$ ) displacement rate.

### 3. Results

The mechanical response measured for single cortical neurons showed marked non-linearities in the strain and strain rate domains and substantial hysteresis, as shown for one representative cell (diameter 14.2  $\mu\text{m}$ , height 7.6  $\mu\text{m}$ ) in Figs. 5 and 6. While these key response features—time/rate dependencies, non-linearities, hysteresis—were consistently observed across the neuronal cell population ( $n = 87$ ), some substantial variations were noted in force magnitude from one cell to the other. The average indentation response and standard deviation are reported in Fig. 7, with the corresponding finite element model fit to the average response. The eight parameter model captures the main characteristics of the cell behavior at large strains, including stress–strain non-linearities, rate effects and long-term time dependencies. Values for the

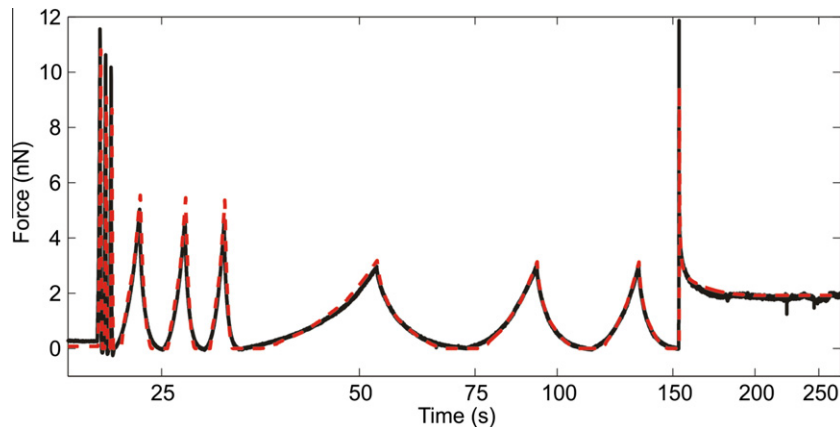


**Fig. 6.** Force versus time responses measured for one representative neuron of diameter 14.2  $\mu\text{m}$  and height 7.6  $\mu\text{m}$  (black) and simulated in Abaqus with actual cell geometry (red dash). Material parameters for this cell were found to be:  $\mu_0 = 13 \text{ Pa}$ ,  $\lambda_L = 1.06$ ,  $G_0 = 85 \text{ Pa}$ ,  $G_\infty = 80 \text{ Pa}$ ,  $\eta = 3000 \text{ Pa s}$ ,  $\sigma_0 = 0.005 \text{ Pa}$ , and  $n = 1$ . Error measure for the model fit was  $1.09 \times 10^{-4}$ .

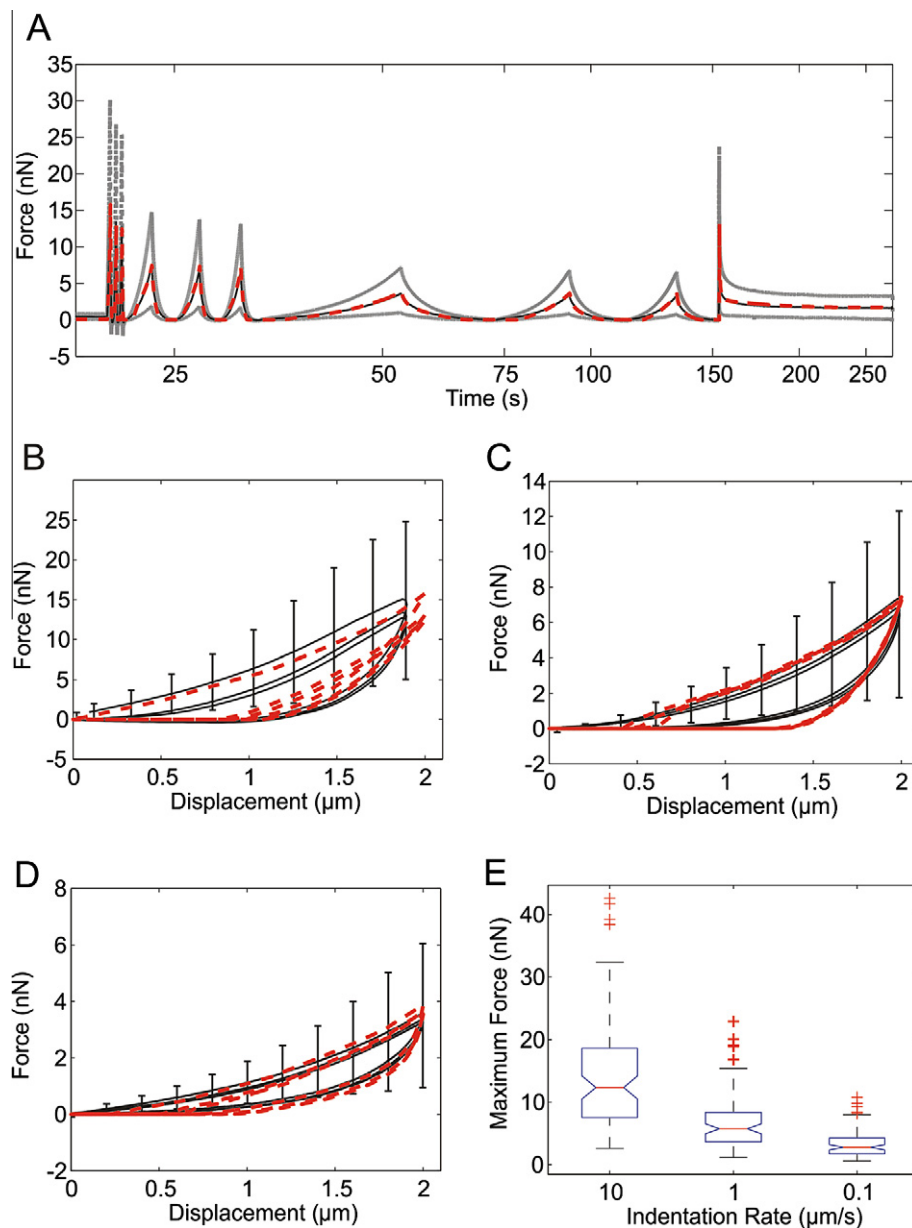


**Fig. 7.** (A) Average force versus time response for 87 cells (black line) with plus and minus standard deviations (grey line); model fit (red dashes) to average response. The pictured model fit corresponds to an error measure of  $1.1 \times 10^{-4}$ . (B–D) Average force versus displacement response at 10, 1 and  $0.1 \mu\text{m s}^{-1}$ , respectively. Error bars represent standard deviations and red dashes correspond to the model fit. (E) Distribution of maximum force level at the end of the first loading ramp for each displacement rate. Outliers are displayed with a red + sign. Rate effects were found to be statistically significant ( $P < 0.0001$ , one-way ANOVA).

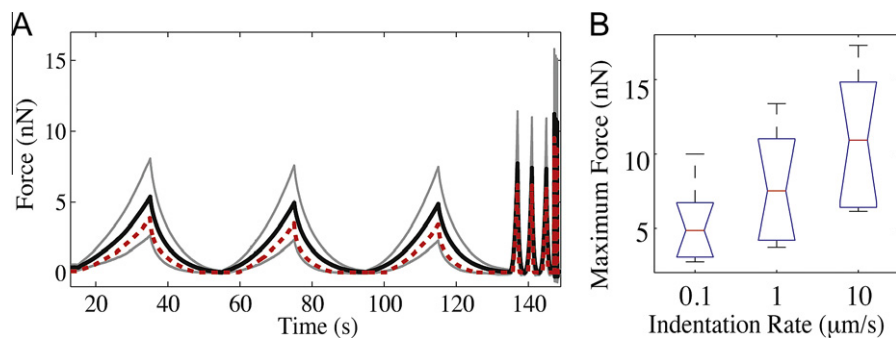


**Fig. 8.** (A) Mean (black) and standard deviation (grey) for 10 neurons indented with loading rates in reverse order ( $0.1$ ,  $1$ , and  $10 \mu\text{m s}^{-1}$ ). Model predictions (red dash) using the set of parameters reported in Fig. 4 corresponding to the model fit shown in Fig. 7. (B) Peak forces reached at the end of the first loading ramp for each displacement rate. Rate effects were found to be significant ( $P < 0.006$ , one-way ANOVA).

**Table 1**

Distribution in parameters (mean and data range) obtained by fitting the model response to experimental data for 33 cells, accounting for actual cell configuration by varying the model geometric parameters to match the measured height and cell radius.

	$G_0$ (Pa)	$n$	$\sigma_0$ (Pa)	$\lambda_L$	$\mu_0$ (Pa)	$\eta$ (Pa s)	$G_\infty$ (Pa)
Mean	78.48	0.9927	0.005455	1.051	15.99	2879	52.64
Range	30–200	0.92–1	0.004–0.009	1.015–1.17	1–75	400–4000	7–300

$K$  was assumed to be constant for all cells and set at 10,000 Pa.

fitting parameters are reported in Fig. 4. Since the AFM data provided a single force–displacement history response, the material bulk and shear contributions to the macroscopic cell response could not be isolated. Following common assumptions of near incompressibility in cell biomechanics, a relatively large value for the bulk modulus, i.e.  $K = 10,000$  Pa, was selected, corresponding to a small strain Poisson's ratio  $\nu = 0.499$ . Note that the set of model parameters associated with the “best” fit is not proven here to be unique, although optimal parameter values are expected to fall within a narrow range. This inference is based on the results of an automated parameter search study conducted by Prevost et al. [58], where the same modeling framework was used to fit the qualitatively similar response of brain tissue.

Upon inversion of the deformation rate order the cell response exhibited similar rate dependencies (Fig. 8). These response features were compared to the model predictions (obtained from the same set of best fit parameters in Fig. 4) and a satisfactory match was found (Fig. 8).

Given the observed wide range of variations in cell geometry, where both cross-diameter and height measurements showed some significant scatter ( $D = 16.8 \pm 2.1$   $\mu\text{m}$ ,  $H = 7.9 \pm 2.0$   $\mu\text{m}$ , mean  $\pm$  SD,  $n = 79$ ), we considered the hypothesis that the deviations in force–indentation response could be mainly ascribed to geometric effects. To investigate the validity of this hypothesis, we performed an approximate geometric normalization for the force indentation responses. A subset of cells ( $n = 33$ ) for which height and cross-diameter estimates could be reliably obtained was selected to generate normalized plots of the cell response, i.e. “nominal stress” versus “nominal strain” diagrams where “nominal stress” and “nominal strain” refer to force and indentation depth normalized by characteristic cross-diameter area and height, respectively. The normalization procedure did not appear to substantially reduce the scatter in the data, indicating that the observed deviations in force–indentation responses might not simply be an effect of cell geometry variations but may also reflect a degree of variability in the constitutive material response.

This conclusion is further supported by the data provided in Table 1, where the best fit model parameters for the subset of cells of known geometrical features ( $n = 33$ ) are given in terms of their average values and ranges of variation. Here, in order to address possible shortcomings of the approximate normalization procedure, sets of model parameters for each cell were obtained by fitting the individual cell responses to finite element models accounting for the actual cell geometry (height and diameter), as shown for one cell in Fig. 6. The mean squared errors between the simulated and measured responses, which ranged between  $7.4 \times 10^{-5}$  and  $1.37 \times 10^{-4}$ , were found to be comparable to those obtained between the simulated and average responses reported earlier in Fig. 6 ( $1.09 \times 10^{-4}$ ) and Fig. 7 ( $1.1 \times 10^{-4}$ ). The scatter in the values of the fitting parameters demonstrate that, even when accurately accounting for cell geometry effects, the cell constitutive response is found to exhibit substantial variability.

Interestingly, in support of an inference of uniqueness for the optimized values, the average of each model parameter obtained by independently fitting data for 33 cells (Table 1) is in good agreement with the corresponding value (Fig. 4) obtained by fitting the representative cell response. From the representative parameters

$G_0 = 75$  Pa,  $G_\infty = 40$  Pa,  $\eta = 3000$  Pa s,  $\sigma_0 = 0.005$  Pa, with a value of  $n = 1$ , it is then possible to estimate short-term and long-term characteristic times for viscous relaxation as  $\tau_0 = 0.67$  s and  $\tau_\infty = 75$  s, with a long-term equilibrium shear modulus  $G_{eq}$  of the order of 25 Pa.

#### 4. Discussion

This study has uncovered novel features pertaining to the large strain dynamic response of single primary neurons of the neonatal rat cortex and presents a general framework for a constitutive model in quantitative support of these observations. It is, to our knowledge, the first reported body of experimental measurements on the nonlinear, hysteretic, viscous behavior of single neural cell somata at finite deformation. The cell response was characterized over three orders of deformation rate magnitude (10, 1, and 0.1  $\mu\text{m s}^{-1}$ ) to 2  $\mu\text{m}$  depth (corresponding to a pseudo-compression nominal strain of 15–40%) in load, unload, and relaxation according to decreasing and increasing orders of deformation rate (10, 1, and 0.1  $\mu\text{m s}^{-1}$  for  $n = 87$  cells, 0.1, 1, and 10  $\mu\text{m s}^{-1}$  for  $n = 10$  cells). The cell response was found to exhibit substantial hysteresis, significant strain, and strain-rate dependent non-linearities, and marked long-term time dependencies. Given the characteristic length scale at which cell properties were probed it is difficult to tease out information about the subcellular, structural basis of the various response features. However, it may be speculated that intermediate filaments and actin filaments are the main contributors to the nonlinear strain dependencies observed at the soma level, as substantiated by previous mechanical investigations on these cytoskeletal components [54,64,65]. Key observations in the response at the single cell level (non-linearities, hysteresis, and time-dependencies) mirror those reported by several investigators at the cortical tissue level [58,66,67] and might pave the way for a unified understanding of the mechanical dynamics unfolding from the tissue level down to the cell level in response to mechanical insults. The corollary observation that the rate effects remain significant upon reversal of the deformation rate order suggests that the dynamic response features measured reflect intrinsic mechanical properties of the cell rather than manifestations of active cellular processes such as cytoskeletal rearrangement (although the involvement of the latter processes cannot be excluded). The present testing protocols may also be adapted/refined to characterize the dynamic properties of other neural cell types and/or cell subregions (e.g. axon hillocks, synaptic boutons, dendritic processes), thereby potentially providing unique insights into mechanically mediated biological responses of single neural cells under complex regimes of deformation. Among the limitations of the current experimental study, we note that the volumetric compliance of the cell and its response in other modes of deformation (tensile, shear) were not investigated. Further, the current experimental method relied on cells plated in vitro on 2D hard substrates. We cannot exclude the possibility that the properties hereby collected differ from those actually encountered in a full 3D environment in vivo. In addition, some significant variations in the mechanical data collected (e.g. peak forces and cell compliances at large strains) were observed within the neuronal



cell population considered ( $n = 87$ ). These differences may be attributed to numerous factors, including potential inaccuracies in the cell–cantilever contact point determination, disparities in cell body geometrical features, variations in cell/substrate contact surface area and adhesion conditions, intrinsic biological differences (cell types, development stages) in the cell population considered, and variation in the initial point of contact relative to the nucleus (which has been shown to be stiffer than its cytoplasmic counterparts [68,69]). These sources of variation may make for interesting avenues of investigation to be explored in future studies. In particular, addressing the question of whether substantial differences in neuron properties exist across brain regions might help unravel the cascade of damage mechanisms suspected to unfold within the brain following the imposition of external mechanical transients.

The constitutive model proposed for the homogenized cell response, following previous continuum developments undertaken at the tissue level [58], was able to capture all major complexities of the cell response in load, unload, reload, and relaxation, via a relatively low number of material parameters. Although phenomenological, the model yielded quantitative assessments of different aspects of the cell response to deformation, e.g. elastic resilience at low to large strains, rate sensitivities in the quasi-static to dynamic regimes. The instantaneous elastic response was found to be well captured by a nonlinear hyperelastic formulation based on a freely jointed chain model, while viscous relaxation was found to be associated with multiple mechanisms, with at least two characteristic times ( $\sim 1$  and  $100$  s) necessary to account for the observed response within the probed range of deformation rates. As refined indicators of cell dynamics, the complete set of model parameters may also elicit subtler discriminations between cell types within and across brain regions, and allow for the establishment of susceptibility to damage maps at the mesoscopic level. These latter considerations may be of particular significance as the potential existence of differential patterns in cell propensity for damage has been substantiated in recent years by observations of consistent mechanical heterogeneities within brain subregions [70]. The current constitutive formulation remains, however, reductive in its simplistic view of the cell as a single, isotropic continuum. The proposed modeling effort must therefore be considered as a preliminary set of constitutive framework developments, potentially enabling the establishment of local stress–strain maps at the cell level, on which structurally based multiscale model refinements may be built.

## Acknowledgements

This work was supported by the US Army Research Office through the MIT Institute for Soldier Nanotechnologies (DAAD-19-02-D0002) and the Joint Improvised Explosive Devices Defeat Organization (W911NF-07-1-0035), the National Science Foundation Graduate Research Fellowship Program, the National Institutes of Health Molecular, Cell, and Tissue Biomechanics Training Grant, the École Nationale des Ponts et Chaussées (Université Paris-Est, France), the Computational Systems Biology Programme of the Singapore–MIT Alliance, and the Interdisciplinary Research Group on Infectious Diseases at the Singapore–MIT Alliance for Research and Technology. The authors are grateful to Professor Sebastian Seung (Massachusetts Institute of Technology, Cambridge, MA) for providing cortical tissue, Professor Patricia Carvalho (Instituto Superior Técnico, Lisbon, Portugal) for imaging SEM samples, and Dr Shelden Yuen and Daniel Rudoy (Harvard University, Cambridge, MA) for providing the MATLAB routine employed in the determination of the cell–cantilever contact point.

## Appendix A. Figures with essential colour discrimination

Certain figures in this article, particularly Figures 6–8, are difficult to interpret in black and white. The full colour images can be found in the on-line version, at doi: [10.1016/j.actbio.2010.10.018](https://doi.org/10.1016/j.actbio.2010.10.018).

## References

- [1] Kraus JF, McArthur DL. Epidemiologic aspects of brain injury. *Neurol Clin* 1996;14:435.
- [2] Tanielian T, Jaycox LH. Invisible wounds of war: psychological and cognitive injuries, their consequences, and services to assist recovery. Santa Monica, CA: RAND Corporation; 2008.
- [3] Hoge CW, Goldberg HM, Castro CA. Care of war veterans with mild traumatic brain injury – flawed perspectives. *N Engl J Med* 2009;360:1588.
- [4] Vanderploeg RD, Curtiss G, Luis CA, Salazar AM. Long-term morbidities following self-reported mild traumatic brain injury. *J Clin Exp Neuropsychol* 2007;29:585.
- [5] Corrigan JD, Selassie AW, Orman JAL. The epidemiology of traumatic brain injury. *J Head Trauma Rehabil* 2010;25:72.
- [6] Belanger HG, Kretzmer T, Yoash-Gantz R, Pickett T, Tupler LA. Cognitive sequelae of blast-related versus other mechanisms of brain trauma. *J Int Neuropsychol Soc* 2009;15:1.
- [7] McCrory P, Makdissi M, Davis G, Collie A. Value of neuropsychological testing after head injuries in football. *Br J Sports Med* 2005;39:158.
- [8] Meehan WP, Bachur RG. Sport-related concussion. *Pediatrics* 2009;123:114.
- [9] Crowe LM, Anderson V, Catroppa C, Babl FE. Head injuries related to sports and recreation activities in school-age children and adolescents: data from a referral centre in Victoria, Australia. *Emerg Med Australas* 2010;22:56.
- [10] Yilmaz S, Pekdemir M. An unusual primary blast injury – traumatic brain injury due to primary blast injury. *Am J Emer Med* 2007;25:97.
- [11] Taber KH, Warden DL, Hurley RA. Blast-related traumatic brain injury: what is known? *J Neuropsychiatry Clin Neurosci* 2006;18:141.
- [12] Lew HL, Poole JH, Alvarez S, Moore W. Soldiers with occult traumatic brain injury. *Am J Phys Med Rehabil* 2005;84:393.
- [13] Bao G, Suresh S. Cell and molecular mechanics of biological materials. *Nat Mater* 2003;2:715.
- [14] Van Vliet K, Bao G, Suresh S. The biomechanics toolbox: experimental approaches for living cells and biomolecules. *Acta Mater* 2003;51:5881.
- [15] Suresh S. Biomechanics and biophysics of cancer cells. *Acta Biomater* 2007;3:413.
- [16] Wang N, Butler JP, Ingber DE. Mechanotransduction across the cell-surface and through the cytoskeleton. *Science* 1993;260:1124.
- [17] Trepatt X, Grabulosa M, Puig F, Maksym GN, Navajas D, Farre R. Viscoelasticity of human alveolar epithelial cells subjected to stretch. *Am J Physiol Lung Cell Mol Physiol* 2004;287:L1025.
- [18] Tagawa H, Wang N, Narishige T, Ingber DE, Zile MR, Cooper G. Cytoskeletal mechanics in pressure-overload cardiac hypertrophy. *Circ Res* 1997;80:281.
- [19] Massiera G, Van Citters KM, Biancaniello PL, Crocker JC. Mechanics of single cells: rheology, time dependence, and fluctuations. *Biophys J* 2007;93:3703.
- [20] Mahaffy RE, Park S, Gerde E, Kas J, Shih CK. Quantitative analysis of the viscoelastic properties of thin regions of fibroblasts using atomic force microscopy. *Biophys J* 2004;86:1777.
- [21] Darling EM, Zauscher S, Guilak F. Viscoelastic properties of zonal articular chondrocytes measured by atomic force microscopy. *Osteoarthritis Cartilage* 2006;14:571.
- [22] Radmacher M, Fritz M, Kacher CM, Cleveland JP, Hansma PK. Measuring the viscoelastic properties of human platelets with the atomic force microscope. *Biophys J* 1996;70:556.
- [23] Mathur AB, Collinsworth AM, Reichert WM, Kraus WE, Truskey GA. Endothelial, cardiac muscle and skeletal muscle exhibit different viscous and elastic properties as determined by atomic force microscopy. *J Biomech* 2001;34:1545.
- [24] Lam W, Rosenbluth M, Fletcher D. Chemotherapy exposure increases leukemia cell stiffness. *Blood* 2007;109:3505.
- [25] Lulevich V, Zink T, Chen HY, Liu FT, Liu GY. Cell mechanics using atomic force microscopy-based single-cell compression. *Langmuir* 2006;22:8151.
- [26] Evans E, Kukan B. Passive material behavior of granulocytes based on large deformation and recovery after deformation tests. *Blood* 1984;64:1028.
- [27] Merryman WD, Youn I, Lukoff HD, Krueger PM, Guilak F, Hopkins RA, et al. Correlation between heart valve interstitial cell stiffness and transvalvular pressure: implications for collagen biosynthesis. *Am J Physiol Heart Circ Physiol* 2006;290:H224.
- [28] Rand RP, Burton AC. Mechanical properties of red cell membrane. I. Membrane stiffness and intracellular pressure. *Biophys J* 1964;4:115.
- [29] Schmidtschonbein GW, Sung KLP, Tozeren H, Skalak R, Chien S. Passive mechanical properties of human leukocytes. *Biophys J* 1981;36:243.
- [30] Sato M, Theret DP, Wheeler LT, Ohshima N, Nerem RM. Application of the micropipette technique to the measurement of cultured porcine aortic endothelial–cell viscoelastic properties. *J Biomech Eng – Trans ASME* 1990;112:263.
- [31] Trickey WR, Vail TP, Guilak F. The role of the cytoskeleton in the viscoelastic properties of human articular chondrocytes. *J Orthop Res* 2004;22:131.

- [32] Henon S, Lenormand G, Richert A, Gallet F. A new determination of the shear modulus of the human erythrocyte membrane using optical tweezers. *Biophys J* 1999;76:1145.
- [33] Mills JP, Diez-Silva M, Quinn DJ, Dao M, Lang MJ, Tan KSW, et al. Effect of plasmodial RESA protein on deformability of human red blood cells harboring *Plasmodium falciparum*. *Proc Natl Acad Sci USA* 2007;104:9213.
- [34] Guck J, Ananthakrishnan R, Mahmood H, Moon TJ, Cunningham CC, Kas J. The optical stretcher: a novel laser tool to micromanipulate cells. *Biophys J* 2001;81:767.
- [35] Lu YB, Franze K, Seifert G, Steinhauser C, Kirchhoff F, Wolburg H, et al. Viscoelastic properties of individual glial cells and neurons in the CNS. *Proc Natl Acad Sci USA* 2006;103:17759.
- [36] Desprat N, Richert A, Simeon J, Asnacios A. Creep function of a single living cell. *Biophys J* 2005;88:2224.
- [37] Fernandez P, Pullarkat PA, Ott A. A master relation defines the nonlinear viscoelasticity of single fibroblasts. *Biophys J* 2006;90:3796.
- [38] Suresh S, Spatz J, Mills JP, Micoulet A, Dao M, Lim CT, et al. Connections between single-cell biomechanics and human disease states: gastrointestinal cancer and malaria. *Acta Biomater* 2005;1:15.
- [39] Binnig G, Quate CF, Gerber C. Atomic force microscope. *Phys Rev Lett* 1986;56:930.
- [40] Franz CM, Puech PH. Atomic force microscopy: a versatile tool for studying cell morphology, adhesion and mechanics. *Cell Mol Bioeng* 2008;1:289.
- [41] Margulies SS, Thibault LE, Gennarelli TA. Physical model simulations of brain injury in the primate. *J Biomech* 1990;23:823.
- [42] Bain AC, Meaney DF. Tissue-level thresholds for axonal damage in an experimental model of central nervous system white matter injury. *J Biomech Eng – Trans ASME* 2000;122:615.
- [43] Zhang LY, Yang KH, King AI. A proposed injury threshold for mild traumatic brain injury. *J Biomech Eng – Trans ASME* 2004;126:226.
- [44] Galbraith JA, Thibault LE, Matteson DR. Mechanical and electrical responses of the squid giant-axon to simple elongation. *J Biomech Eng – Trans ASME* 1993;115:13.
- [45] Li QS, Lee GYH, Ong CN, Lim CT. AFM indentation study of breast cancer cells. *Biochem Biophys Res Commun* 2008;374:609.
- [46] Spagnoli C, Beyder A, Besch SR, Sachs F. Drift-free atomic force microscopy measurements of cell height and mechanical properties. *Rev Sci Instrum* 2007;78.
- [47] Radmacher M. Studying the mechanics of cellular processes by atomic force microscopy. *Cell Mech* 2007;83:347.
- [48] Costa KD, Sim AJ, Yin FCP. Non-Hertzian approach to analyzing mechanical properties of endothelial cells probed by atomic force microscopy. *J Biomech Eng – Trans ASME* 2006;128:176.
- [49] Karcher H, Lammerding J, Huang HD, Lee RT, Kamm RD, Kaazempur-Mofrad MR. A three-dimensional viscoelastic model for cell deformation with experimental verification. *Biophys J* 2003;85:3336.
- [50] Unnikrishnan GU, Unnikrishnan VU, Reddy JN. Constitutive material modeling of cell: a micromechanics approach. *J Biomech Eng – Trans ASME* 2007;129:315.
- [51] Shin D, Athanasiou K. Cytoindentation for obtaining cell biomechanical properties. *J Orthop Res* 1999;17:880.
- [52] Guilak F, Mow VC. The mechanical environment of the chondrocyte: a biphasic finite element model of cell–matrix interactions in articular cartilage. *J Biomech* 2000;33:1663.
- [53] McGarry JG, Prendergast PJ. A three-dimensional finite element model of an adherent eukaryotic cell. *Eur Cell Mater* 2004;7:27.
- [54] Gardel ML, Nakamura F, Hartwig JH, Crocker JC, Stossel TP, Weitz DA. Prestressed F-actin networks cross-linked by hinged filamins replicate mechanical properties of cells. *Proc Natl Acad Sci USA* 2006;103:1762.
- [55] Brewer G, Torricelli J. Isolation and culture of adult neurons and neurospheres. *Nat Protoc* 2007;2:1490.
- [56] Matei GA, Thoreson EJ, Pratt JR, Newell DB, Burnham NA. Precision and accuracy of thermal calibration of atomic force microscopy cantilevers. *Rev Sci Instrum* 2006;77.
- [57] Rudy D, Yuen S, Howe R, Wolfe PJ. Bayesian changepoint analysis with application to atomic force microscopy and soft material indentation. *J Roy Stat Soc Ser C* 2010;59:573.
- [58] Prevost TP, Balakrishnan A, Suresh S, Socrate S. Biomechanics of brain tissue. *Acta Biomater* 2011;7:83.
- [59] Gurtin ME. An introduction to continuum mechanics. New York: Academic Press; 1981.
- [60] Holzapfel GA. Nonlinear solid mechanics: a continuum approach for engineering. Chichester: Wiley; 2000.
- [61] Lee E. Elastic–plastic deformation at finite strains. *J Appl Mech* 1969;36:1.
- [62] Arruda E, Boyce M. A three-dimensional constitutive model for the large stretch behavior of rubber elastic materials. *J Mech Phys Solids* 1993;41:389.
- [63] Bergstrom J, Boyce M. Constitutive modeling of the time-dependent and cyclic loading of elastomers and application to soft biological tissues. *Mech Mater* 2001;33:523.
- [64] Storm C, Pastore JJ, MacKintosh FC, Lubensky TC, Janmey PA. Nonlinear elasticity in biological gels. *Nature* 2005;435:191.
- [65] Xu JY, Tseng Y, Wirtz D. Strain hardening of actin filament networks – regulation by the dynamic cross-linking protein alpha-actinin. *J Biol Chem* 2000;275:35886.
- [66] Miller K, Chinzei K. Constitutive modelling of brain tissue: experiment and theory. *J Biomech* 1997;30:1115.
- [67] Franceschini G, Bigoni D, Regitnig P, Holzapfel G. Brain tissue deforms similarly to filled elastomers and follows consolidation theory. *J Mech Phys Solids* 2006;54:2592.
- [68] Guilak F, Tedrow JR, Burgkart R. Viscoelastic properties of the cell nucleus. *Biochem Biophys Res Commun* 2000;269:781.
- [69] Maniotis A, Chen C, Ingber D. Demonstration of mechanical connections between integrins, cytoskeletal filaments, and nucleoplasm that stabilize nuclear structure. *Proc Natl Acad Sci USA* 1997;94:849.
- [70] Elkin B, Azeloglu E, Costa K, Morrison Iii B. Mechanical heterogeneity of the rat hippocampus measured by atomic force microscope indentation. *J Neurotrauma* 2007;24:812.